

Structure transition and zigzag magnetic order in Ir/Rh-substituted honeycomb lattice α -RuCl₃

Zachary Morgan,¹ Iris Ye,² Colin L. Sarkis,¹ Xiaoping Wang,¹ Stephen Nagler,^{1,3} and Jiaqiang Yan⁴

¹Neutron Scattering Division, Oak Ridge National Laboratory, Oak Ridge, Tennessee 37831, USA

²Next Generation STEM Internship Program Participant

³Department of Physics and Astronomy, University of Tennessee, Knoxville, Tennessee 37996, USA

⁴Materials Science and Technology Division, Oak Ridge National Laboratory, Oak Ridge, Tennessee 37831, USA

(Dated: October 5, 2023)

We report magnetization and neutron diffraction studies on crystal and magnetic structures of Ir- and Rh-substituted honeycomb lattice α -RuCl₃. The iridium or rhodium atoms are distributed at the Ru site with little structural modification. Both systems undergo a room-temperature monoclinic $C2/m$ to low-temperature trigonal $R\bar{3}$ phase transformation with a large recoverable hysteresis. At low temperature, a zigzag spin order is observed with the same characteristic wavevector $(0, 0.5, 1)$ as in the parent α -RuCl₃. Detailed magnetic structure refinement reveals an ordered moment of $0.32(5)\mu_B/\text{Ru}$ and an upper boundary of canting angle of $15(4)^\circ$ away from the basal plane at 5 K for the 10% Ir-substituted α -RuCl₃, which is different from the $0.45\text{-}0.73\mu_B/\text{Ru}$ and $32^\circ\text{-}48^\circ$ canting angle reported in the parent compound α -RuCl₃. The observation of unchanged RuCl₆ local octahedral environment, reduced magnetic moment size and canting angle highlights the potential to study quantum spin liquid behavior through non-magnetic ion doping.

INTRODUCTION

The interplay between topology and electron correlation leads to a large variety of interesting topological phenomena in quantum materials. These include fractional quantum Hall effect where the quasi-particles carry a fraction of the electron charge [1, 2] and quantum spin liquid (QSL) where the quantum fluctuations prevent magnetic order down to absolute zero temperature [3, 4]. The Kitaev spin model on a honeycomb lattice [5] is an exactly solvable example in which spin dynamics fractionalizes into itinerant Majorana fermions and Ising gauge-field excitations. The experimental realization for this model was initially proposed in quasi-2D iridates A₂IrO₃ [6], where the bond directional Ising interactions arise from spin-orbit-assisted $j_{\text{eff}} = 1/2$ state in an edge-sharing environment. Recent focus has gradually shifted to the honeycomb lattice α -RuCl₃ [7, 8]. Despite the apparent appearance of long-range magnetic order, both inelastic neutron scattering and Raman spectroscopy [9–12] have detected a broad scattering continuum in α -RuCl₃. This continuum aligns with the predicted presence of itinerant Majorana fermion and is interpreted as indicating that α -RuCl₃ is situated in close proximity to the QSL state. Additionally, anomalous thermal Hall properties are observed in the QSL state with applied in-plane magnetic fields [13–16].

Below $T_N = 7$ K, α -RuCl₃ exhibits a zigzag spin structure [17–19] like what was observed in honeycomb iridates [20–22]. The static spin configuration is quite fragile and susceptible to various perturbations including in-plane magnetic field [12, 23, 24], hydrostatic pressure [25–27], stacking disorder [18, 28], and chemical substitution [29–31]. In the latter case, partial substitution of Ru³⁺ with magnetic Cr³⁺ ions destabilizes the zig-zag long-range magnetic order and favors a spin-glass state [30]. Alternatively, the inclusion of non-magnetic ions such as Rh³⁺ [31] and Ir³⁺ [29] seems to only suppress the zigzag order without any signature of freezing into a spin glass state. Furthermore, inelastic neutron scatter-

ing studies have found that the key character of fractionalized excitations is maintained in a wide range of Ir concentration even when the long-range spin order is absent [29]. This is particularly intriguing as it reveals the robust nature in the dynamical channel and provides a viable route to achieve the long-sought-after quantum spin liquid state in the absence of applied magnetic field.

The impact of chemical substitution on the crystal and magnetic structures of α -RuCl₃ has not been thoroughly studied before partially due to the availability of sizable single crystals. In this work, the growth, magnetic properties, nuclear and magnetic structures of Ru_{1-x}R_xCl₃ ($R = \text{Ir, Rh}$) single crystals are reported. With a moderate concentration of $x = 0.1$, the transition temperature T_N is suppressed to around 6 K. A large hysteresis about 70 K is present between the room temperature (T) monoclinic $C2/m$ and the low- T trigonal $R\bar{3}$ crystal structures likely due to the presence of stacking disorder. As observed in α -RuCl₃, both systems revert to the room temperature monoclinic structure after thermal cycling without sign of stacking disorder evident as diffuse scattering along the c^* -axis. A significant reduced moment of $0.32(5)\mu_B/\text{Ru}$ is observed in the Ir-substituted α -RuCl₃ zigzag spin configuration. The spin moment is in the ac -plane with tilting angle $15(4)^\circ$ away from the a -axis [the direction perpendicular to the Ru-Ru bond]. Both moment size and canting angle are smaller than previous reports in α -RuCl₃ with moment size of $0.45\text{-}0.73\mu_B/\text{Ru}$ and canting angle of $35\text{-}48^\circ$ [17, 18].

EXPERIMENTAL DETAILS

Single crystals of Rh- and Ir-substituted α -RuCl₃ were prepared using self-selecting vapor growth method [32]. The commercial RuCl₃ powder from Furuya Metals (Japan) was used in the growths without further purification. Pure RhCl₃ and IrCl₃ powders were obtained by reacting the transition

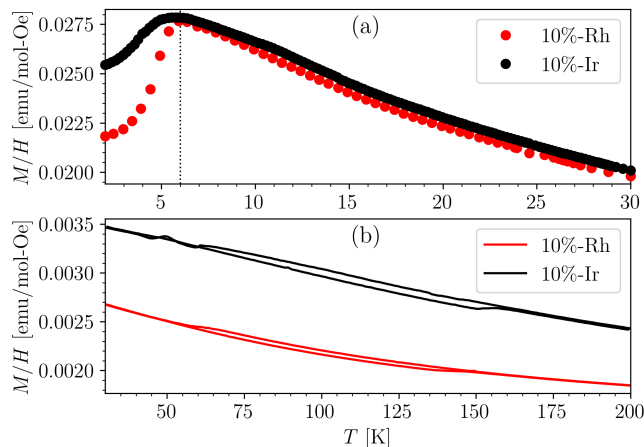


FIG. 1. Temperature dependence of magnetization of 10% Ir- and Ru-substituted α - RuCl_3 . (a) Low temperature magnetization highlighting the magnetic ordering temperature. The data were collected in a magnetic field of 1 kOe along an arbitrary direction in ab -plane. (b) High temperature magnetization highlighting the structural transition at high temperatures. The measurement is performed with a ramping rate of 2 K/min in a magnetic field of 10 kOe applied perpendicular to the plate.

metal oxides with AlCl_3 -KCl salt [33]. Plate-like crystals with a typical in-plane dimension of 5-10 mm and thickness up to 1 mm can be obtained. Magnetic properties were measured with a Quantum Design (QD) Magnetic Property Measurement System in the temperature range 2.0-300 K. The compositions of the crystals were determined using energy dispersive spectroscopy (EDS) with a Hitachi TM3000 scanning electron microscope and Bruker Quantax70 spectrometer. EDS suggests the transition metal/chlorine ratio is 1:3. However, the significant overlap of peaks prevents a reliable determination of the real composition. Therefore, nominal composition is used in this work. Magnetic measurements were used to screen crystals for further characterizations. We noticed some variation of magnetic and structural transitions among crystals from the same batch, indicating the variation of substitution content. Therefore, magnetic and neutron diffraction measurements were performed on the same piece of crystals for each composition.

Neutron diffraction experiments of 10% substituted compositions were carried out using the single crystal diffractometer CORELLI [34] at the Spallation Neutron Source (SNS) to study both the crystal and magnetic structures and the corresponding structural transition. Individual crystals were glued to a thin aluminum plate and loaded inside a closed-cycle refrigerator with a base temperature of 5 K. The neutron diffraction data are first collected at 200 K (above the structural transition) with 360 degrees of rotation about the vertical axis. After samples were cooled to base temperature, another full map was collected to investigate the magnetic structure. The crystals were then warmed back to 200 K to probe possible structural change after thermal cycling. During initial cooling

and subsequent warming, characteristic Bragg peaks that are unique to the specific space group of the crystal were closely monitored as function of temperature with a ramping rate of 1 K/min.

A similar single crystal neutron diffraction experiment of 20% Rh-substituted samples were also performed on the TOPAZ diffractometer [35, 36] at SNS. Crystals were attached via GE varnish to thin aluminum posts with the monoclinic a^* axis oriented vertically. Sample temperature was controlled by a Cryomech P415 pulse tube cryocooler and data were collected using sample orientations optimized for coverage with the CrystalPlan software [37]. Data were taken above the structural transition at 250 K as well as below the structural transitions at base temperature of 15 K. Crystals were cooled and heated at a rate of 2 K/min and the transitions were tracked studying the nominal $(1, 1, 3)$ Bragg peak of the low temperature $R\bar{3}$ structure.

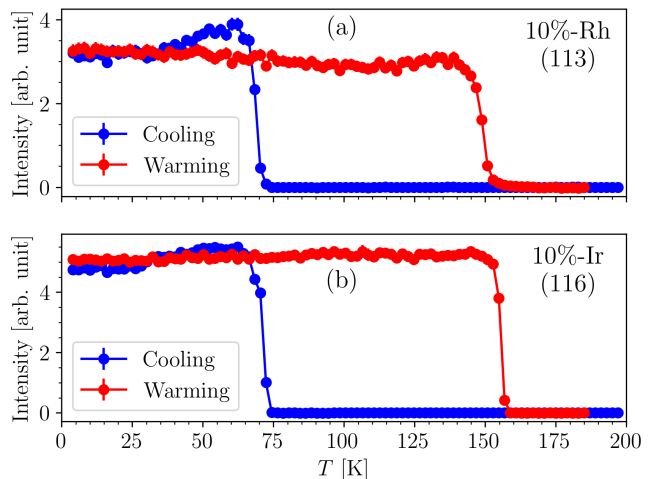


FIG. 2. Cooling (blue) and warming (red) curves of integrated peak intensity for (a) 10% Rh-substituted and (b) 10% Ir-substituted α - RuCl_3 showing large hysteresis in structure transformation between high-temperature $C2/m$ monoclinic and low-temperature $R\bar{3}$ trigonal structure. The first order transition is complete and does not exhibit remnant phase coexistence at low temperature.

RESULTS AND DISCUSSION

The temperature-dependent magnetization of 10% Ru- and Ir-substituted α - RuCl_3 crystals used for neutron diffraction study at CORELLI is shown in Fig. 1. Both samples exhibit a long-range magnetic order with similar $T_N = 6$ K. The different magnitudes of the magnetization drop below T_N may result from different in-plane field directions. A weak hump around 10 K is observed for the Ir-substituted crystals, indicating the presence of stacking disorder in this piece of crystal. The higher temperature magnetization shown in 1(b) highlights the structure transition. For both compositions, the transition occurs around 60 K upon cooling and 150 K upon

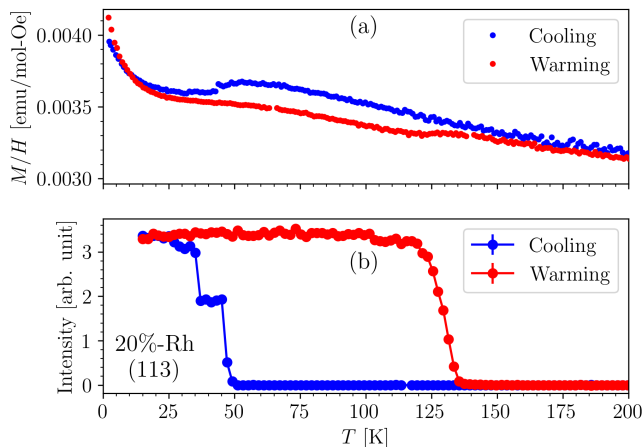


FIG. 3. Temperature dependence of (a) magnetization and (b) intensity of (1, 1, 3) reflection of 20% Rh-substituted α -RuCl₃. Magnetic data were collected with a ramping rate of 2 K/min in a magnetic field of 1 T applied perpendicular to the crystal plate. No long range magnetic order is observed above 2 K while the structure transition is still present.

warming, resulting in a wide loop in the temperature dependent magnetization.

The presence of the structure transition is further confirmed by neutron diffraction study. Structural refinement indicates that the substituted α -RuCl₃ systems crystallize in a monoclinic $C2/m$ space group at room temperature and transforms to trigonal $R\bar{3}$ space group at low temperature consistent with other reports in crystals without doping [38, 39]. Figure 2(a) shows the T -dependence of the nuclear reflection (1, 1, 3) indexed in the low- T $R\bar{3}$ space group upon cooling and warming. The abrupt increase in intensity near 75 K of this peak on cooling and sudden disappearance at 150 K on warming confirms the transition is first order and is consistent with previous investigation on the pure α -RuCl₃ where the temperature difference of the structural transition between cooling and warming critically depends on the degree of stacking disorder [39]. A narrower hysteresis window typically implies the single crystal contains smaller amount of stacking disorder. The large hysteresis windows observed in Figs. 1 and 2 might reflect increased stacking disorder. It is yet to be investigated whether the stacking disorder comes from inappropriate growth parameters or chemical substitution.

In parent α -RuCl₃, the structure transition occurs around 170 K upon warming. In contrast, our observations in this study indicate a transition temperature roughly 20 K lower for 10% Rh or Ir substituted compositions. This reduction in the structure transition temperature appears to be a consequence of chemical substitution. Figure 3(a) shows the temperature dependence of magnetization of 20% Rh-substituted RuCl₃. No long range magnetic order was observed above 2 K for this composition. The thermal evolution of the (1, 1, 3) peaks shown in Fig. 3(b) indicates the structure transition occurs around 50 K upon cooling and 130 K upon warming. Both

temperatures are consistent with those obtained from magnetic measurements. It is worth noting that the transition temperature upon warming is further reduced compared to those for 10% Rh or Ir-substituted compositions. This indicates that the nonmagnetic substitution in the honeycomb plane affects not only the in-plane magnetic interactions but the inter-layer coupling. Despite the apparent difference in the thermal hysteresis, the structural parameters among all substituted α -RuCl₃ samples from structure refinement remains unchanged compared to the parent compound. The lattice constants, bond distances, and bond angles are nearly the same within uncertainty (see Appendix). This could be expected as the effective ionic radii of and Rh³⁺ is 0.665 Å, similar to Ir³⁺ and Ru³⁺ that are identical at 0.68 Å [40].

The difference between the room temperature monoclinic $C2/m$ phase shown in Fig. 4(a) and low- T trigonal $R\bar{3}$ phase shown in Fig. 4(b) can be visualized in the reciprocal space mappings that are displayed Fig. 4(c)-Fig. 4(h). Lattice parameter determination from observed structural Bragg peaks indicates room temperature monoclinic cell parameters with base centering conditions. At low temperature, a hexagonal cell is observed with peaks indexed with rhombohedral lattice centering. Each space group can be confirmed through detailed analysis of the Bragg intensities using least squares refinement. More details about the structure refinements and Bragg integration are given in the Appendix. In the room temperature phase, the honeycomb layers are stacked in an arrangement corresponding to a simple translation along the c -axis with displacement vector perpendicular to the armchair of the honeycomb bond that is illustrated in Fig. 4(a). In the case of the low- T trigonal phase, the stacking sequence is different as shown in Fig. 4(b). Viewing from the direction perpendicular to the basal plane, the neighboring layers are separated by an in-plane displacement vector of $[2/3a, 1/3a]$ which is 60° from the armchair bond.

Figures 4(c)-4(h) show the reciprocal space contour maps for both crystals at 200 K (pristine), 5 K (cooled), and 200 K (warmed) conditions. The $C2/m \rightarrow R\bar{3}$ structural transition induces notable structural diffuse scattering in the low-temperature phase. The line-cuts across a Bragg peak along the c^* -direction in Figs. 4(d) and 4(g) for Rh-doping and Ir-doping, respectively, show clear Lorentzian profile with a full width half maximum approximately 0.1 reciprocal lattice unit indicating a correlation length of 155 ± 5 Å. However, the samples fully recover the original states after thermal cycling evidenced by the sharp Bragg reflections and the lack of rod-like feature along the c^* -direction. For the crystal with Rh-doping, this is shown in Figs. 4(c) and 4(e) that can be compared to the crystal with Ir-doping shown Figs. 4(f) and 4(h). Two distinct sets of Bragg intensities are in the low temperature trigonal phase: one strong and the other weak. The strong set is from the major structural domain which fulfills the rhombohedral obverse setting ($-h + k + l = 3n$). The weaker set originates from a twinned domain generated by a two-axis rotation about the $[1, \bar{1}, 0]$ -direction of the major domain in the reverse setting ($h - k + l = 3n$). This type of

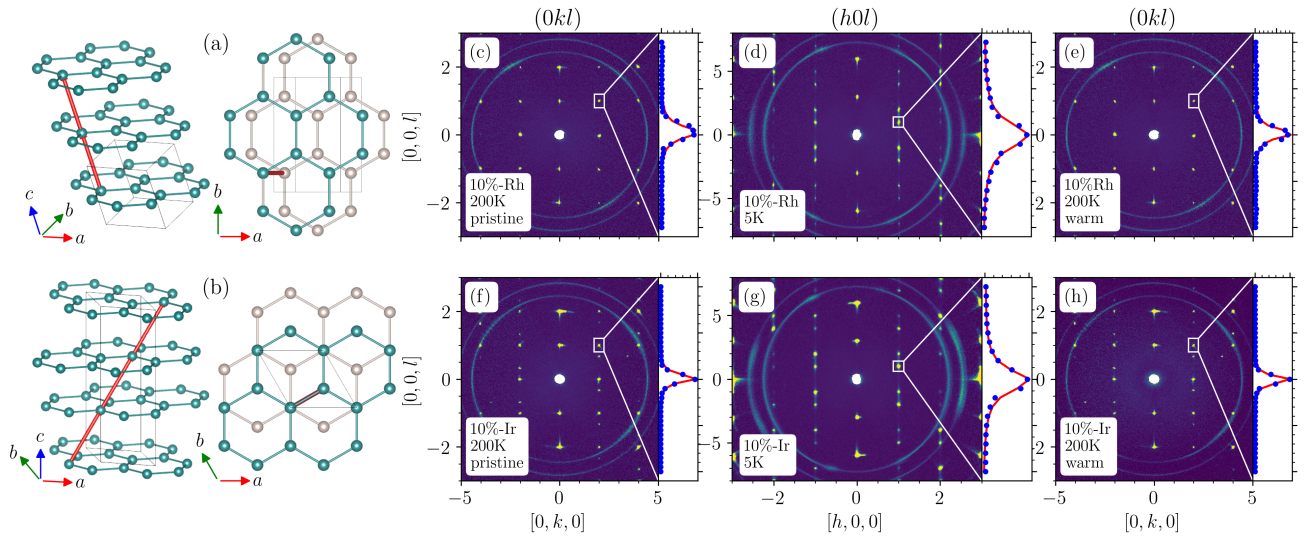


FIG. 4. Stacking sequence of honeycomb layers in (a) $C2/m$ and (b) $R\bar{3}$ space groups. The out-of-plane stacking shift vector is $[0, 0, 1]$ and $[2/3, 1/3, 1/3]$, respectively. Heatmap plot of 10% Rh-substituted α - RuCl_3 at (c) 200 K on first cooling, (d) 5 K, and (e) 200 K after warming. Similar data collected for 10% Ir-substituted α - RuCl_3 at (f) 200 K on cooling, (g) 5 K, and (h) 200 K on warming. Both Rh- and Ir-substituted crystals are indexed using monoclinic $C2/m$ space group at high temperature while the low- T data are indexed in the hexagonal $R\bar{3}$ space group. Note both systems recover to the pristine state showing absence of structural diffuse scattering after thermal cycling back to 200 K. For the Ir-substituted sample, the appearance of an additional domain can be indexed using a twin with 120° rotation about the c^* -axis. This domain recovers after thermal cycling. The inset shows selected line-cuts along the c^* -axis with sharp Bragg peaks in the monoclinic phase and broad peaks with diffuse scattering along c^* in the trigonal setting.

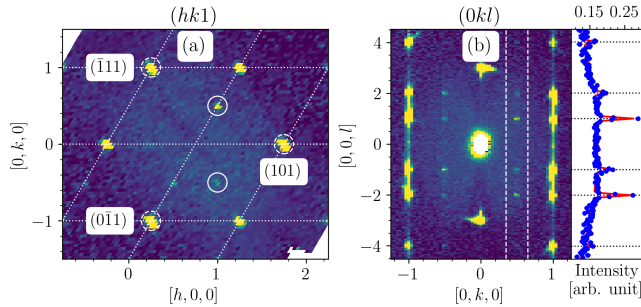


FIG. 5. (a) Intensity slice in the $(h, k, 1)$ plane showing the magnetic satellite peaks with propagation wavevector $(0, 0.5, 1)$ for the 10% Ir-substituted α - RuCl_3 at $T = 5.0$ K. Two structural domains correspond to obverse/reverse twinning with volume ratio of 77:23. Structural peaks from the major domain are highlighted in dashed white circles. The magnetic twins associated with the major structural domain are evident with 120° rotation along c^* and marked in closed white circles. Note that the axes are skewed according to the 60° angle between a^* and b^* . (b) The intensity slice in the $(0, k, l)$ plane. Magnetic reflections are present at $k = \pm 0.5$ with $l = \pm 1, \pm 2$ and ± 4 . The line-cut across $k = 0.5$ shows a distinct distribution of intensities corresponding to the two structural domains.

obverse/reverse twinning is found to occur in the $R\bar{3}$ space group [41]. The population ratio is 77:23. A proper identification of this ratio is important for determining the spin configuration that relies on an accurate account of all structural and magnetic domain contributions.

Both 10% substituted compositions enter a magnetic or-

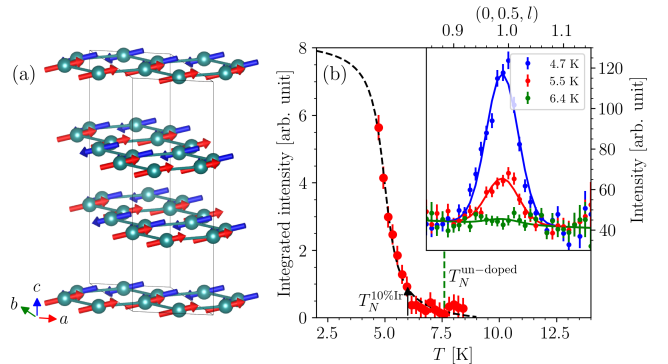


FIG. 6. (a) Refined zigzag spin structure of 10% Ir-substituted α - RuCl_3 at $T = 5.0$ K. The magnetic moments are aligned in the ac plane with a canting angle of $15(4)^\circ$ away from the basal plane. (b) The temperature dependence of the integrated intensity of the $(0, 0.5, 1)$ magnetic reflection. The dashed line is guide to eye. The inset shows selective cuts across the magnetic transition.

dered state at low temperature. The characteristic propagation vector $(0, 0.5, 1)$ is the same as that reported in the parent α - RuCl_3 [17, 19] but different from the sample that retains a low- T monoclinic structure [28]. A complete reciprocal space map is necessary to elucidate the coexisting structural and magnetic domains for a reliable determination of the magnetic structure. Figure 5(a) shows the $(h, k, l = 1)$ slice of the 10% Ir-substituted sample at 5 K. For the major structural domain, there could exist three magnetic twins that are

120° apart along the c^* -axis, since the magnetic wavevector breaks the three-fold symmetry. For this domain, two strong magnetic reflections located at $(0, 0.5, 1)$ and $(0.5, -0.5, 1)$ are visible and highlighted in closed circles. A third magnetic domain originating from the major structural domain is hardly visible at the expected $(-0.5, 0, 1)$ peak position. By contrast, the minor structural domain shows one distinct magnetic peak at $(0, -0.5, 1)$. Figure 5(b) shows the $(h = 0, k, l)$ slice where the magnetic satellite peaks are present at $k = \pm 0.5$. The line-cut along the $[0, 0, l]$ -direction shows markedly strong intensities at $l = -2, 1$ and 4, while the weak reflections at remaining l values come from the minor structural domain. Two structural domains are also observed in the 10% Rh-substituted sample at 5 K. The magnetic reflections can also be indexed with the same $(0, 0.5, 1)$ wavevector, but the magnetic signal is too weak due to lower counting statistics for proper extraction of the magnetic intensities needed for structure refinement. More details related to 10% Rh-substituted sample are given in the Appendix.

The magnetic space group compliant with the wavevector $(0, 0.5, 1)$ and Ru-ion at the $6c$ site in the parent $R\bar{3}$ space group is P_S-1 (#2.7 BNS setting). Although the magnetic cell doubles the unit cell along the b -axis, there is only one magnetic site with a - and c -axis components to be determined for the zigzag spin structure. Given that magnetic intensity measurements probe the spin component perpendicular \mathbf{S}_\perp to the momentum transfer \mathbf{Q} [$\mathbf{S}_\perp = \mathbf{Q} \times (\mathbf{S} \times \mathbf{Q})$], a comprehensive examination of out-of-plane l components in the surveyed magnetic reflections $(0, 0.5, l = 1 + 3n)$ further constrains the spin canting angles. A sizable intensity at $l = 4$ implies the spin component is directed closer to the ab -plane. Together with magnetic reflections from other twinned magnetic domains, magnetic structure refinement of the Ir-substituted sample using Fullprof [42] results in a zigzag structure with spin canting angle slightly away from the basal plane. The goodness of fit remains relatively flat for the canting angle between -15° to 15° but increases sharply beyond these values. This sets an upper boundary for the canting angle. A more detailed analysis is given in the Appendix. The ordered moment is determined to be $0.32(5) \mu_B/\text{Ru}$ at 5 K and the resulting spin configuration is illustrated in Fig. 6(a). The thermal evolution of the integrated $(0, 0.5, 1)$ peak intensity is shown in Fig. 6(b) where the Néel temperature is observed near 6 K and is consistent with the magnetic susceptibility study in Fig. 1(a). An earlier study of pure $\alpha\text{-RuCl}_3$ [17] reported an ordered moment of $0.73 \mu_B/\text{Ru}$ at 4 K with canting angle of 48° from the a -axis. The moment at 5 K from this report based on the change in magnetic Bragg peak is estimated to be $0.69 \mu_B/\text{Ru}$. In a separate independent study, the moment size at 4.2 K is determined to be $0.45(5) \mu_B/\text{Ru}$ with canting angle 35° away from the honeycomb plane [18]. This indicates the magnetic moment size of the Ir-substituted $\alpha\text{-RuCl}_3$ sample observed in this study is smaller than that reported in the parent compound $\alpha\text{-RuCl}_3$.

The spin direction is crucial to understand the strength of relative interactions and nature of the zigzag order. Since

the discovery of $\alpha\text{-RuCl}_3$ as one of the promising candidates realizing Kitaev quantum spin liquid, extensive efforts have focused on identifying a proper microscopic model that is capable of capturing the essential features of the inelastic neutron scattering and bulk property data [43–49]. A combined analysis of various experimental observations has converged on a minimal generalized Kitaev-Heisenberg Hamiltonian (K - J - Γ - Γ' - J_3) encompassing Ising-like Kitaev interaction K , Heisenberg exchange J , symmetric off-diagonal exchange coupling Γ, Γ' , and the third-neighbor Heisenberg coupling J_3 [50–57]. The Kitaev term K for $\alpha\text{-RuCl}_3$ is generally considered to be ferromagnetic [11, 51, 52, 58] and it is believed the zigzag order is stabilized by either longer-range antiferromagnetic couplings J_3 or anisotropic off-diagonal Γ and Γ' terms [50]. A sufficiently strong anisotropic term Γ leads to a moment locked in the ac -crystallographic plane while the introduction of Γ' , usually small and originating from trigonal compression, lowers the critical threshold of Γ required to stabilize the moment. The canting angle α away from the honeycomb plane can be analytically expressed as $\tan 2\alpha = 4/\sqrt{2}(1+r)/(7r-2)$ where $r = -\Gamma/(K + \Gamma')$ [22, 50]. The canting angle obtained in this study serves as a valuable constraint for understanding the relative strength of the terms K, Γ , and Γ' in further studies of the microscopic models of substituted $\alpha\text{-RuCl}_3$.

Furthermore, our structure investigation reveals minimal alteration of the lattice parameters and average local RuCl_6 environment when compared to the parent compound $\alpha\text{-RuCl}_3$ (see Appendix). The trigonal crystal electric field arising from compression of the RuCl_6 octahedra, plays a pivotal role in stabilizing the zigzag order evidenced from the strong anisotropic magnetization [59], akin to observations in iridates [60]. The absence of significant changes in these structural parameters suggests the suppression of both the transition temperature and ordered moment comes factors other than chemical pressure [31] or alterations of crystalline electric field. One possible contributing factor could be the disruption of exchange pathways due to the dilution of the honeycomb lattice. On the other hand, the inelastic neutron scattering spectra have shown that the spin liquid state in $\text{Ru}_{1-x}\text{Ir}_x\text{Cl}_3$ is robust against iridium doping; the low- T characteristic upper excitation feature associated with the fractionalized excitations is present in a wide range of non-magnetic iridium doping even when the static spin order is completely absent [29]. This is in line with the recent theoretical study where the introduction of nonmagnetic vacancy concentrations preserves most of the spin-liquid behavior [61]. The vacancies contribute to a pileup of Majorana modes accumulated in the density of states, which can be experimentally verified by future low- T specific heat measurements.

SUMMARY

In summary, we use neutron single crystal diffraction to determine the crystal and magnetic structure of honeycomb

lattice α -RuCl₃ with Ru partially substituted by nonmagnetic Rh³⁺ and Ir³⁺ ions. Similar to α -RuCl₃, both 10% substituted samples exhibit a zigzag magnetic order with an identical characteristic magnetic wavevector below T_N , undergo a first-order structural transition from room-temperature $C2/m$ to low-temperature $R\bar{3}$ phase, fully revert to their original $C2/m$ state after undergoing thermal cycling. An examination of the nuclear structure suggests that the substitution of Ir/Rh does not introduce any significant alterations in either the average structure or the local environment of the RuCl₆ octahedra. However, both the magnetic order and the structural transition upon warming are observed to occur at lower temperatures in these chemically substituted samples, indicating the nonmagnetic impurities affect both the in-plane magnetic interactions and the interlayer coupling. The magnetic structure refinement conducted in the Ir-substituted sample has revealed a reduction in both the magnetic moment size and canting angle when compared to the values reported earlier for α -RuCl₃. These findings provide valuable constraints for future theoretical investigations into the magnetic Hamiltonian in substituted α -RuCl₃. Chemical substitution with nonmagnetic ions of similar atomic radii presents an attractive approach for tailoring the magnetic properties of materials in close proximity to a quantum spin liquid state.

ACKNOWLEDGMENTS

IY was supported by an appointment to the Oak Ridge National Laboratory (ORNL) Next Generation STEM Internship Program (NGSI) Program, sponsored by the U.S. Department of Energy and administered by the Oak Ridge Institute for Science and Education. This research was supported by the U.S. Department of Energy (DOE), Office of Science, National Quantum Information Science Research Centers, Quantum Science Center and used resources at the Spallation Neutron Source, a DOE Office of Science User Facility operated by ORNL. All drawings of crystal and magnetic structures were obtained using VESTA software [62]. This manuscript has been authored by UT-Battelle, LLC, under Contract No. DE-AC0500OR22725 with the U.S. Department of Energy.

APPENDIX

Structural Analysis

Nuclear Bragg peaks of the sample are integrated in reciprocal space and corrected with Lorentz and spectrum corrections [63]. Using a best-fitting three dimensional ellipsoid envelope, the resulting intensities are corrected for wavelength-dependent absorption [64] of the sample using an equivalent sphere analytical correction [65] with chemical formula Ru_{0.9}Rh_{0.1}Cl₃ ($R = \text{Ir, Rh}$), unit cell Z -parameter and volume. The Mantid software is used throughout the data reduction process [66]. In the Jana crystal structure refinements,

the twin law corresponding to obverse/reverse twinning is introduced with variable domain population. A wavelength-dependent secondary spherical extinction correction model is applied [67]. Structure refinement of the calculated structure factors to the corrected Bragg intensities from the complete reciprocal space maps are used to refine the positions of the Ru and Cl-sites. Determination of the exact doping level is difficult due to the typical broadening of Bragg peaks observed in van der Waals materials. In addition, the scattering length of Rh is somewhat closer to Ru than Ir. For the 10%-samples measured at CORELLI, the compositions are determined to be 6-7% for Ir-doped sample and 11% for Rh-doped sample. Subsequent refinements to obtain the bond distances and angles are done with composition fixed at $x = 0.1$. For the TOPAZ Rh-doped sample with the nominal composition of $x = 0.2$, the sample composition is determined to be 22% Rh..

TABLE I. Structural parameters at high and low temperature phases for the doped α -RuCl₃ compared to un-doped one. Note uncertainties of lattice constant are standard errors. Lengths are in angstroms and angles are in degrees

$C2/m$	10%-Rh	20%-Rh	10%-Ir	parent [39]
a	6.000(5)	5.980(1)	5.981(3)	5.976(1)
b	10.331(4)	10.348(1)	10.344(2)	10.343(1)
c	6.0092(2)	6.0356(1)	6.027(1)	6.023(1)
β	108.74(5)	108.72(1)	108.88(2)	108.80(1)
$R\bar{3}$	10%-Rh	20%-Rh	10%-Ir	parent [17]
a	5.973(3)	5.974(1)	5.972(1)	5.973(1)
c	16.956(9)	16.961(2)	16.953(3)	16.93(6)

Table I lists the lattice parameters of both the high temperature $C2/m$ and low temperature $R\bar{3}$ phases. The parameters for all compositions appear similar. For the monoclinic case, a reference sample previously measured on CORELLI at 200 K is reported [39]. In the case of the trigonal phase, the parameters at 5 K from [17] are used for comparison. For clarity, the $R\bar{3}$ space group has a hexagonal unit cell with R rhombohedral lattice centering. Structural refinement analysis is performed using Jana2020 [68] to obtain the refined site fractional coordinates. Typical bond-distances, and angles of the RuCl₆ octahedra are reported in Table II. In this table, the superscript indicates a symmetry operator of the site that forms the bond. No superscript indicates the identity operator (x, y, z). There does not appear to be a significant difference among all samples studied. The low temperature reference values for the trigonal case are also from [17] at 5 K.

Magnetic Structure Analysis

The zigzag magnetic structure corresponds to irreducible representation Γ_1 . The basis vectors from representation analysis are shown in Table III for the Ru ion and used in the Full-Prof refinement [42]. Magnetic peaks from the Ir-substituted sample are integrated in a similar fashion to the structural

TABLE II. Selected Ru-Cl bond distances and angles at high and low temperature phases for the doped α -RuCl₃ compared to un-doped one. Note uncertainties are standard errors. Lengths are in angstroms and angles are in degrees.

$C2/m$	10%-Rh	20%-Rh	10%-Ir	parent [39]
Ru1-Cl1	2.360(2)	2.363(1)	2.361(2)	2.363(1)
Ru1-Cl2	2.358(2)	2.361(1)	2.361(2)	2.361(1)
Ru1-Cl2 ⁱⁱ	2.359(2)	2.359(1)	2.359(2)	2.359(1)
$R\bar{3}$	10%-Rh	20%-Rh	10%-Ir	parent [17]
Ru1-Cl1	2.363(3)	2.361(4)	2.362(1)	2.359(6)
Ru1-Cl1 ^{III}	2.356(2)	2.360(3)	2.359(1)	2.352(6)
$C2/m$	10%-Rh	20%-Rh	10%-Ir	parent [39]
Cl1-Ru1-Cl1 ⁱ	86.50(7)	86.27(3)	86.37(5)	86.48(2)
Cl1-Ru1-Cl2	91.30(7)	91.61(3)	91.48(6)	91.55(2)
Cl1-Ru1-Cl2 ⁱ	91.49(7)	91.10(3)	91.25(6)	91.20(2)
Cl1-Ru1-Cl2 ⁱⁱ	91.14(6)	91.30(2)	91.33(4)	91.24(2)
Cl2-Ru1-Cl2 ⁱⁱ	85.58(6)	85.99(2)	85.92(4)	86.01(2)
Cl2-Ru1-Cl2 ⁱⁱⁱ	91.75(6)	91.40(2)	91.46(4)	91.35(2)
Cl2 ⁱⁱ -Ru1-Cl2 ⁱⁱⁱ	91.36(7)	91.28(3)	91.11(5)	91.18(2)
$R\bar{3}$	10%-Rh	20%-Rh	10%-Ir	parent [17]
Cl1-Ru1-Cl1 ^I	91.39(6)	91.56(8)	91.58(2)	91.36(2)
Cl1-Ru1-Cl1 ^{III}	86.09(5)	86.12(8)	86.15(2)	85.90(2)
Cl1-Ru1-Cl1 ^V	91.24(5)	91.24(8)	91.17(2)	91.61(1)
Cl1 ^{III} -Ru1-Cl1 ^{IV}	91.39(6)	91.18(8)	91.21(2)	91.26(2)

Superscript indicates symmetry operator. Unlabeled refers to (x, y, z) .

$C2/m$: ⁱ $(-x, y, -z + 1)$, ⁱⁱ $(-x + 1/2, -y + 1/2, -z + 1)$,

ⁱⁱⁱ $(x - 1/2, -y + 1/2)$; $R\bar{3}$: ^I $(-y, x - y, z)$, ^{II} $(-x + y, -x, z)$,

^{III} $(-x + 1/3, -y + 2/3, -z + 2/3)$, ^{IV} $(y - 2/3, -x + y - 1/3, -z + 2/3)$,

^V $(x - y + 1/3, x - 1/3, -z + 2/3)$

TABLE III. Basis vectors of irreducible representation of zigzag magnetic structure with the Ru 6c site.

Γ_1	ψ_1	ψ_2	ψ_3
Ru $(0, 0, z)$	$(1, 0, 0)$	$(0, 1, 0)$	$(0, 0, 1)$
Ru $(0, 0, \bar{z})$	$(\bar{1}, 0, 0)$	$(0, \bar{1}, 0)$	$(0, 0, \bar{1})$

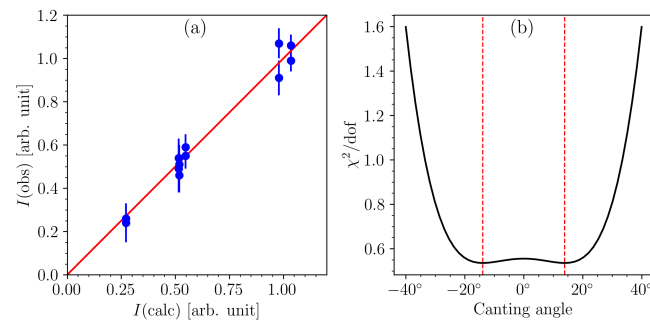


FIG. 7. (a) The observed to calculated intensities with canting angle that minimizes the χ^2 from 12 magnetic peaks. The solid red line is guide to the eye. (b) Dependence of fitted χ^2 per degree of freedom with canting angle comparing observed integrated intensities to calculated structure factors for the 10% Ir-substituted sample. Canting angle shows a clear minimum near 15° denoted with the dashed red line.

Bragg peaks. Six magnetic peaks from each structural domain

are integrated. The primary domain with 77% contribution contains the magnetic reflections that are offset from indexed nuclear peaks in the rhombohedrally centered obverse setting. The secondary domain with 23% has peaks indexed from the reverse twin as discussed in the text. To determine the moment size, the magnetic peaks are refined with the Bragg reflections to obtain the scale factor.

The observed magnetic intensities are compared to the expected values for the refined structure are shown in Fig. 7(a) for the Ir-substituted sample with canting angle 15° . The χ^2 goodness of fit per degree of freedom (dof) with variable canting angle from the magnetic structural model is shown in Fig. 7(b) and shows a clear minimum near 15° . Above 15° (and below -15°), the χ^2 deviates drastically. Hence, 15° is the upper bound of the canting angle. As the change in χ^2 is small about zero canting angle within ± 15 does not rule out smaller canting angles within uncertainty.

The order parameter of the Ir-substituted $(0, 0.5, 1)$ magnetic satellite peak integrated intensity is compared to reference data for the parent compound [17, 18] in Fig. 8. The intensities of the reference data are scaled by a factor to the guide line. For reference [17] with un-substituted crystal structure determined in space group $R\bar{3}$, it is estimated that the moment size of the parent compound at 5 K data will be about $0.69 \mu_B/\text{Ru}$ which is associated with an approximately 10% drop in intensity from the value at 4 K estimated from the intensity reduction of the order parameter. A reduction of intensity by a factor is associated with a corresponding change of moment size by the square root of that factor since intensities scale with the square of the magnetic structure factor. Similarly, for reference [18] with magnetic structure determined in parent space group $C2/m$, the associated drop in intensity is approximately 5% at 5K indicating a minor change in moment size (approximately $0.46 \mu_B/\text{Ru}$). This suggests the magnetic moment size of the Ir-substituted sample is smaller than these previous reports.

As the Rh-doped sample has a similar reverse/obverse structural twinning with one major and minor domain, the appearance of magnetic peaks follows a similar trend with the Ir-doped sample. The $(0, k, l)$ intensity slice from the Rh-doped sample at 5 K is displayed in Fig. 9 and shows magnetic peaks appearing at similar positions as the Ir-doped sample out to $l = \pm 4$ which include $(0, 0.5, \pm 1)$, $(0, 0.5, \pm 2)$, and $(0, 0.5, \pm 4)$. Magnetic peaks can also be observed along the $[0, -0.5, l]$ direction. Due to counting statistics, the magnetic peaks are too weak for reliable integration and magnetic structure refinement.

- [1] X. Du, I. Skachko, F. Duerr, A. Luican, and E. Y. Andrei, Fractional quantum Hall effect and insulating phase of Dirac electrons in graphene, *Nature* **462**, 192 (2009).
- [2] K. I. Bolotin, F. Ghahari, M. D. Shulman, H. L. Stormer, and P. Kim, Observation of the fractional quantum Hall effect in graphene, *Nature* **462**, 196 (2009).

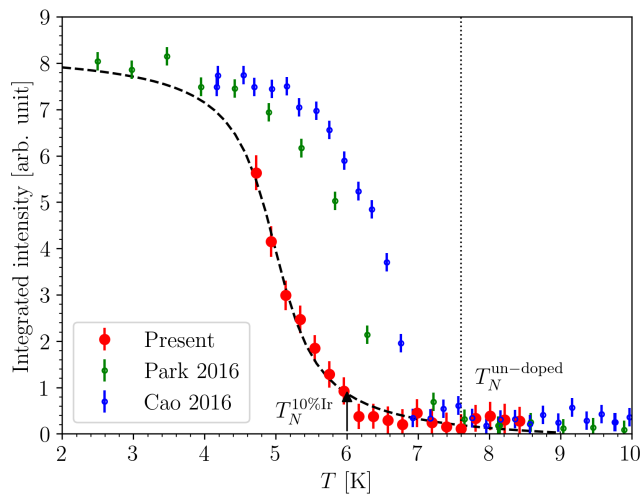


FIG. 8. Comparison of the thermal evolution of the 10% Ir-substituted $(0, 0.5, 1)$ magnetic satellite peak to order parameters from references [17, 18] corresponding to un-substituted α -RuCl₃. The intensity values of the reference data are scaled to the guide line. The transition of the present data appears lower than the parent material.

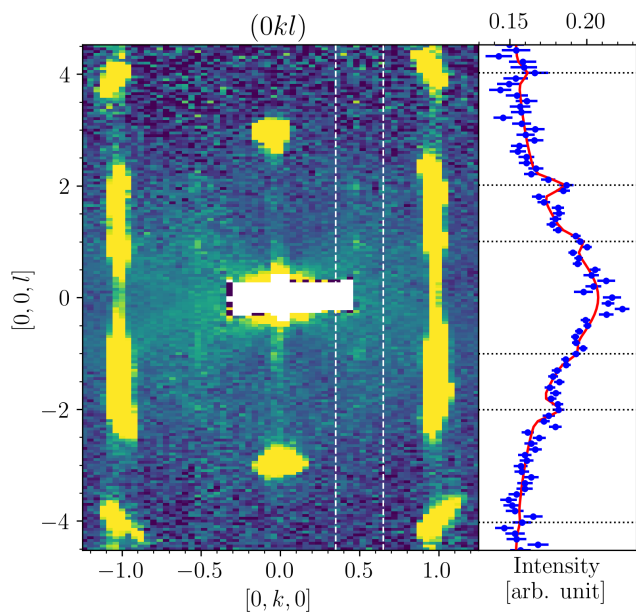


FIG. 9. The intensity slice in the $(0, k, l)$ plane from the 10% Rh-substituted sample. Magnetic reflections are present but appear weaker than observed in 10% Ir-doping at $k = \pm 0.5$ with $l = \pm 1, \pm 2$ and ± 4 .

[3] L. Balents, Spin liquids in frustrated magnets, *Nature* **464**, 199 (2010).
 [4] K. Kitagawa, T. Takayama, Y. Matsumoto, A. Kato, R. Takano, Y. Kishimoto, S. Bette, R. Dinnebier, G. Jackeli, and H. Takagi, A spin-orbital-entangled quantum liquid on a honeycomb lattice, *Nature* **554**, 341 (2018).
 [5] A. Kitaev, Anyons in an exactly solved model and beyond, *Annals of Physics* **321**, 2 (2006).

[6] G. Jackeli and G. Khaliullin, Mott Insulators in the Strong Spin-Orbit Coupling Limit: From Heisenberg to a Quantum Compass and Kitaev Models, *Physical Review Letters* **102**, 017205 (2009).
 [7] K. W. Plumb, J. P. Clancy, L. J. Sandilands, V. V. Shankar, Y. F. Hu, K. S. Burch, H.-Y. Kee, and Y.-J. Kim, α -RuCl₃: A spin-orbit assisted Mott insulator on a honeycomb lattice, *Physical Review B* **90**, 041112 (2014).
 [8] H. Takagi, T. Takayama, G. Jackeli, G. Khaliullin, and S. E. Nagler, Concept and realization of kitaev quantum spin liquids, *Nature Reviews Physics* **1**, 264 (2019).
 [9] L. J. Sandilands, Y. Tian, K. W. Plumb, Y.-J. Kim, and K. S. Burch, Scattering Continuum and Possible Fractionalized Excitations in α -RuCl₃, *Physical Review Letters* **114**, 147201 (2015).
 [10] J. Nasu, J. Knolle, D. L. Kovrizhin, Y. Motome, and R. Moessner, Fermionic response from fractionalization in an insulating two-dimensional magnet, *Nature Physics* **12**, 912 (2016).
 [11] A. Banerjee, C. A. Bridges, J.-Q. Yan, A. A. Aczel, L. Li, M. B. Stone, G. E. Granroth, M. D. Lumsden, Y. Yiu, J. Knolle, S. Bhattacharjee, D. L. Kovrizhin, R. Moessner, D. A. Tennant, D. G. Mandrus, and S. E. Nagler, Proximate Kitaev quantum spin liquid behaviour in a honeycomb magnet, *Nature Materials* **15**, 733 (2016).
 [12] A. Banerjee, P. Lampen-Kelley, J. Knolle, C. Balz, A. A. Aczel, B. Winn, Y. Liu, D. Pajerowski, J. Yan, C. A. Bridges, A. T. Savici, B. C. Chakoumakos, M. D. Lumsden, D. A. Tennant, R. Moessner, D. G. Mandrus, and S. E. Nagler, Excitations in the field-induced quantum spin liquid state of α -RuCl₃, *npj Quantum Materials* **3**, 1 (2018).
 [13] Y. Kasahara, T. Ohnishi, Y. Mizukami, O. Tanaka, S. Ma, K. Sugii, N. Kurita, H. Tanaka, J. Nasu, Y. Motome, T. Shibauchi, and Y. Matsuda, Majorana quantization and half-integer thermal quantum Hall effect in a Kitaev spin liquid, *Nature* **559**, 227 (2018).
 [14] T. Yokoi, S. Ma, Y. Kasahara, S. Kasahara, T. Shibauchi, N. Kurita, H. Tanaka, J. Nasu, Y. Motome, C. Hickey, S. Trebst, and Y. Matsuda, Half-integer quantized anomalous thermal Hall effect in the Kitaev material candidate α -RuCl₃, *Science* **373**, 568 (2021).
 [15] J. A. N. Bruin, R. R. Claus, Y. Matsumoto, N. Kurita, H. Tanaka, and H. Takagi, Robustness of the thermal Hall effect close to half-quantization in α -RuCl₃, *Nature Physics* (2022).
 [16] P. Czajka, T. Gao, M. Hirschberger, P. Lampen-Kelley, A. Banerjee, N. Quirk, D. G. Mandrus, S. E. Nagler, and N. P. Ong, Planar thermal Hall effect of topological bosons in the Kitaev magnet α -RuCl₃, *Nature Materials* **22**, 36 (2023).
 [17] S.-Y. Park, S.-H. Do, K.-Y. Choi, D. Jang, T.-H. Jang, J. Schefer, C.-M. Wu, J. S. Gardner, J. M. S. Park, J.-H. Park, and S. Ji, Emergence of the Isotropic Kitaev Honeycomb Lattice with Two-dimensional Ising Universality in α -RuCl₃, 2016, 1609.05690.
 [18] H. B. Cao, A. Banerjee, J.-Q. Yan, C. A. Bridges, M. D. Lumsden, D. G. Mandrus, D. A. Tennant, B. C. Chakoumakos, and S. E. Nagler, Low-temperature crystal and magnetic structure of α -RuCl₃, *Physical Review B* **93**, 134423 (2016).
 [19] C. Balz, L. Janssen, P. Lampen-Kelley, A. Banerjee, Y. H. Liu, J.-Q. Yan, D. G. Mandrus, M. Vojta, and S. E. Nagler, Field-induced intermediate ordered phase and anisotropic interlayer interactions in α -RuCl₃, *Physical Review B* **103**, 174417 (2021).
 [20] S. K. Choi, R. Coldea, A. N. Kolmogorov, T. Lancaster, I. I. Mazin, S. J. Blundell, P. G. Radaelli, Y. Singh, P. Gegenwart, K. R. Choi, S.-W. Cheong, P. J. Baker, C. Stock, and J. Tay-

- lor, Spin Waves and Revised Crystal Structure of Honeycomb Iridate Na₂IrO₃, *Physical Review Letters* **108**, 127204 (2012).
- [21] F. Ye, S. Chi, H. Cao, B. C. Chakoumakos, J. A. Fernandez-Baca, R. Custelcean, T. F. Qi, O. B. Korneta, and G. Cao, Direct evidence of a zigzag spin-chain structure in the honeycomb lattice: A neutron and x-ray diffraction investigation of single-crystal Na₂IrO₃, *Physical Review B* **85**, 180403 (2012).
- [22] J. Chaloupka, G. Jackeli, and G. Khaliullin, Zigzag Magnetic Order in the Iridium Oxide Na₂IrO₃, *Physical Review Letters* **110**, 097204 (2013).
- [23] J. A. Sears, Y. Zhao, Z. Xu, J. W. Lynn, and Y.-J. Kim, Phase Diagram of α -RuCl₃ in an in-plane Magnetic Field, *Physical Review B* **95**, 180411 (2017).
- [24] S.-H. Baek, S.-H. Do, K.-Y. Choi, Y. S. Kwon, A. U. B. Wolter, S. Nishimoto, J. van den Brink, and B. Büchner, Evidence for a Field-Induced Quantum Spin Liquid in α -RuCl₃, *Physical Review Letters* **119**, 037201 (2017).
- [25] B. Wolf, D. A. S. Kaib, A. Razpopov, S. Biswas, K. Riedl, S. M. Winter, R. Valentí, Y. Saito, S. Hartmann, E. Vinokurova, T. Doert, A. Isaeva, G. Bastien, A. U. B. Wolter, B. Büchner, and M. Lang, Combined experimental and theoretical study of hydrostatic He-gas pressure effects in α -RuCl₃, *Physical Review B* **106**, 134432 (2022).
- [26] X. Wang, F. Zhu, N. Qureshi, K. Beauvois, J. Song, T. Mueller, T. Brückel, and Y. Su, Hydrostatic pressure effects in the Kitaev quantum magnet RuCl₃: A single-crystal neutron diffraction study, 2023, 2304.00632.
- [27] P. Bhattacharyya, L. Hozoi, Q. Stahl, J. Geck, and N. A. Bogdanov, Sweet spot in the RuCl₃ magnetic system: Nearly ideal jeff = 1/2 moments and maximized K/J ratio under pressure, 2023, 2302.00540.
- [28] R. D. Johnson, S. C. Williams, A. A. Haghighirad, J. Singleton, V. Zapf, P. Manuel, I. I. Mazin, Y. Li, H. O. Jeschke, R. Valentí, and R. Coldea, Monoclinic crystal structure of α -RuCl₃ and the zigzag antiferromagnetic ground state, *Physical Review B* **92**, 235119 (2015).
- [29] P. Lampen-Kelley, A. Banerjee, A. A. Aczel, H. B. Cao, M. B. Stone, C. A. Bridges, J.-Q. Yan, S. E. Nagler, and D. Mandrus, Destabilization of Magnetic Order in a Dilute Kitaev Spin Liquid Candidate, *Physical Review Letters* **119**, 237203 (2017).
- [30] G. Bastien, M. Roslova, M. H. Haghighi, K. Mehlawat, J. Hunger, A. Isaeva, T. Doert, M. Vojta, B. Büchner, and A. U. B. Wolter, Spin-glass state and reversed magnetic anisotropy induced by Cr doping in the Kitaev magnet α -RuCl₃, *Physical Review B* **99**, 214410 (2019).
- [31] G. Bastien, E. Vinokurova, M. Lange, K. K. Bestha, L. T. C. Bohorquez, G. Kreutzer, A. Lubk, T. Doert, B. Büchner, A. Isaeva, and A. U. B. Wolter, Dilution of the magnetic lattice in the Kitaev candidate α -RuCl₃ by Rh³⁺ doping, *Physical Review Materials* **6**, 114403 (2022).
- [32] J.-Q. Yan and M. A. McGuire, Self-selecting vapor growth of transition-metal-halide single crystals, *Physical Review Materials* **7**, 013401 (2023).
- [33] J.-Q. Yan, B. C. Sales, M. A. Susner, and M. A. McGuire, Flux growth in a horizontal configuration: An analog to vapor transport growth, *Physical Review Materials* **1**, 023402 (2017).
- [34] F. Ye, Y. Liu, R. Whitfield, R. Osborn, and S. Rosenkranz, Implementation of cross correlation for energy discrimination on the time-of-flight spectrometer CORELLI, *Journal of Applied Crystallography* **51**, 315 (2018).
- [35] A. J. Schultz, M. R. V. Jørgensen, X. Wang, R. L. Mikkelsen, D. J. Mikkelsen, V. E. Lynch, P. F. Peterson, M. L. Green, and C. M. Hoffmann, Integration of neutron time-of-flight single-crystal bragg peaks in reciprocal space, *Journal of Applied Crystallography* **47**, 915 (2014).
- [36] L. Coates et al., A suite-level review of the neutron single-crystal diffraction instruments at oak ridge national laboratory, *Review of Scientific Instruments* **89** (2018).
- [37] J. Zikovsky, P. F. Peterson, X. P. Wang, M. Frost, and C. Hoffmann, Crystalplan: an experiment-planning tool for crystallography, *Journal of Applied Crystallography* **44**, 418 (2011).
- [38] S. Mu, K. D. Dixit, X. Wang, D. L. Abernathy, H. Cao, S. E. Nagler, J. Yan, P. Lampen-Kelley, D. Mandrus, C. A. Polanco, L. Liang, G. B. Halász, Y. Cheng, A. Banerjee, and T. Berlijn, Role of the third dimension in searching for Majorana fermions in α -RuCl₃ via phonons, *Physical Review Research* **4**, 013067 (2022).
- [39] H. Zhang, M. A. McGuire, A. F. May, J. Chao, Q. Zheng, M. Chi, B. C. Sales, D. G. Mandrus, S. E. Nagler, H. Miao, F. Ye, and J. Yan, Stacking disorder and thermal transport properties of α -RuCl₃, 2023, 2303.03682.
- [40] R. D. Shannon, Revised effective ionic radii and systematic studies of interatomic distances in halides and chalcogenides, *Acta Cryst A* **32**, 751 (1976).
- [41] R. Herbst-Irmer and G. M. Sheldrick, Refinement of obverse/reverse twins, *Acta Cryst B* **58**, 477 (2002).
- [42] J. Rodríguez-Carvajal, Recent advances in magnetic structure determination by neutron powder diffraction, *Physica B: Condensed Matter* **192**, 55 (1993).
- [43] K. Ran, J. Wang, W. Wang, Z.-Y. Dong, X. Ren, S. Bao, S. Li, Z. Ma, Y. Gan, Y. Zhang, J. T. Park, G. Deng, S. Danilkin, S.-L. Yu, J.-X. Li, and J. Wen, Spin-Wave Excitations Evidencing the Kitaev Interaction in Single Crystalline α -RuCl₃, *Physical Review Letters* **118**, 107203 (2017).
- [44] S. M. Winter, K. Riedl, P. A. Maksimov, A. L. Chernyshev, A. Honecker, and R. Valentí, Breakdown of magnons in a strongly spin-orbital coupled magnet, *Nature Communications* **8**, 1152 (2017).
- [45] L. Wu, A. Little, E. E. Aldape, D. Rees, E. Thewalt, P. Lampen-Kelley, A. Banerjee, C. A. Bridges, J.-Q. Yan, D. Boone, S. Patankar, D. Goldhaber-Gordon, D. Mandrus, S. E. Nagler, E. Altman, and J. Orenstein, Field evolution of magnons in α -RuCl₃ by high-resolution polarized terahertz spectroscopy, *Physical Review B* **98**, 094425 (2018).
- [46] T. Cookmeyer and J. E. Moore, Spin-wave analysis of the low-temperature thermal Hall effect in the candidate Kitaev spin liquid α -RuCl₃, *Physical Review B* **98**, 060412 (2018).
- [47] P. Lampen-Kelley, S. Rachel, J. Reuther, J.-Q. Yan, A. Banerjee, C. A. Bridges, H. B. Cao, S. E. Nagler, and D. Mandrus, Anisotropic susceptibilities in the honeycomb Kitaev system α -RuCl₃, *Physical Review B* **98**, 100403 (2018).
- [48] I. O. Ozel, C. A. Belvin, E. Baldini, I. Kimchi, S. Do, K.-Y. Choi, and N. Gedik, Magnetic field-dependent low-energy magnon dynamics in α -RuCl₃, *Physical Review B* **100**, 085108 (2019).
- [49] J. A. Sears, L. E. Chern, S. Kim, P. J. Berciarua, S. Francoual, Y. B. Kim, and Y.-J. Kim, Ferromagnetic Kitaev interaction and the origin of large magnetic anisotropy in α -RuCl₃, *Nature Physics* **16**, 837 (2020).
- [50] J. Chaloupka and G. Khaliullin, Magnetic anisotropy in the Kitaev model systems Na₂IrO₃ and RuCl₃, *Physical Review B* **94**, 064435 (2016).
- [51] H.-S. Kim and H.-Y. Kee, Crystal structure and magnetism in α -RuCl₃: An ab initio study, *Physical Review B* **93**, 155143 (2016).
- [52] S. M. Winter, Y. Li, H. O. Jeschke, and R. Valentí, Challenges in design of Kitaev materials: Magnetic interactions from competing energy scales, *Physical Review B* **93**, 214431 (2016).

- [53] Y. S. Hou, H. J. Xiang, and X. G. Gong, Unveiling magnetic interactions of ruthenium trichloride via constraining direction of orbital moments: Potential routes to realize a quantum spin liquid, *Physical Review B* **96**, 054410 (2017).
- [54] W. Wang, Z.-Y. Dong, S.-L. Yu, and J.-X. Li, Theoretical investigation of magnetic dynamics in α -RuCl₃, *Physical Review B* **96**, 115103 (2017).
- [55] C. Eichstaedt, Y. Zhang, P. Laurell, S. Okamoto, A. G. Eguiluz, and T. Berlijn, Deriving models for the Kitaev spin-liquid candidate material α -RuCl₃ from first principles, *Physical Review B* **100**, 075110 (2019).
- [56] P. A. Maksimov and A. L. Chernyshev, Rethinking α -RuCl₃, *Physical Review Research* **2**, 033011 (2020).
- [57] P. Laurell and S. Okamoto, Dynamical and thermal magnetic properties of the Kitaev spin liquid candidate α -RuCl₃, *npj Quantum Materials* **5**, 2 (2020).
- [58] L. Wu, A. Little, E. E. Aldape, D. Rees, E. Thewalt, P. Lampen-Kelley, A. Banerjee, C. A. Bridges, J.-Q. Yan, D. Boone, S. Patankar, D. Goldhaber-Gordon, D. Mandrus, S. E. Nagler, E. Altman, and J. Orenstein, Field evolution of magnons in α -RuCl₃ by high-resolution polarized terahertz spectroscopy, *Physical Review B* **98**, 094425 (2018).
- [59] Y. Kubota, H. Tanaka, T. Ono, Y. Narumi, and K. Kindo, Successive magnetic phase transitions in α -RuCl₃: XY-like frustrated magnet on the honeycomb lattice, *Physical Review B* **91**, 094422 (2015).
- [60] H. Gretarsson, J. P. Clancy, X. Liu, J. P. Hill, E. Bozin, Y. Singh, S. Manni, P. Gegenwart, J. Kim, A. H. Said, D. Casa, T. Gog, M. H. Upton, H.-S. Kim, J. Yu, V. M. Katukuri, L. Hozoi, J. van den Brink, and Y.-J. Kim, Crystal field splitting and correlation effect on the electronic structure of A2IrO₃, *Physical Review Letters* **110**, 076402 (2013).
- [61] W.-H. Kao, J. Knolle, G. B. Halász, R. Moessner, and N. B. Perkins, Vacancy-Induced Low-Energy Density of States in the Kitaev Spin Liquid, *Physical Review X* **11**, 011034 (2021).
- [62] K. Momma and F. Izumi, VESTA 3 for three-dimensional visualization of crystal, volumetric and morphology data, *J Appl Cryst* **44**, 1272 (2011).
- [63] T. M. Michels-Clark, A. T. Savici, V. E. Lynch, X. Wang, and C. M. Hoffmann, Expanding Lorentz and spectrum corrections to large volumes of reciprocal space for single-crystal time-of-flight neutron diffraction, *J Appl Crystallogr* **49**, 497 (2016).
- [64] V. F. Sears, Neutron scattering lengths and cross sections, *Neutron News* **3**, 26 (1992).
- [65] C. W. Dwiggin, Rapid calculation of X-ray absorption correction factors for spheres to an accuracy of 0.05%, *Acta Cryst A* **31**, 395 (1975).
- [66] O. Arnold et al., Mantid—Data analysis and visualization package for neutron scattering and μ SR experiments, *Nuclear Instruments and Methods in Physics Research Section A: Accelerators, Spectrometers, Detectors and Associated Equipment* **764**, 156 (2014).
- [67] P. J. Becker and P. Coppens, Extinction within the limit of validity of the Darwin transfer equations. II. Refinement of extinction in spherical crystals of SrF₂ and LiF, *Acta Cryst A* **30**, 148 (1974).
- [68] V. Petříček, L. Palatinus, J. Plášil, and M. Dušek, Jana2020 – a new version of the crystallographic computing system Jana, *Zeitschrift für Kristallographie - Crystalline Materials* **238**, 271 (2023).